Evaluating the Influence of Hemorheological Parameters on Circulating Tumor Cell Trajectory and Simulation Time

Sayan Roychowdhury
sayan.roychowdhury@duke.edu
Duke University
Durham, NC, USA

John Gounley
gounleyjp@ornl.gov
Oak Ridge National Laboratory
Oak Ridge, TN, USA

Amanda Randles
amanda.randles@duke.edu
Duke University
Durham, NC, USA

ABSTRACT

Extravasation of circulating tumor cells (CTCs) occurs primarily in the microvasculature, where flow and cell interactions significantly affect the blood rheology. Capturing cell trajectory at this scale requires the coupling of several interaction models, leading to increased computational cost that scales as more cells are added or the domain size is increased. In this work, we focus on micro-scale vessels and study the influence of certain hemorheological factors, including the presence of red blood cell aggregation, hematocrit level, microvessel size, and shear rate, on the trajectory of a circulating tumor cell. We determine which of the aforementioned factors significantly affect CTC motion and identify those which can potentially be disregarded, thus reducing simulation time. We measure the effect of these elements by studying the radial CTC movement and runtime at various combinations of these hemorheological parameters. To accurately capture blood flow dynamics and single cell movement, we perform high-fidelity hemodynamic simulations at a sub-micron resolution using our in-house fluid dynamics solver, HARVEY. We find that increasing hematocrit increases the likelihood of tumor cell margination, which is exacerbated by the presence of red blood cell aggregation. As microvessel diameter increases, there is no major CTC movement towards the wall; however, including aggregation causes the CTC to marginate quicker as the vessel size increases. Finally, as the shear rate is increased, the presence of aggregation has a diminished effect on tumor cell margination.

KEYWORDS

lattice Boltzmann, immersed boundary, red blood cell aggregation, cell tracking, microvasculature

ACM Reference Format:
Sayan Roychowdhury, John Gounley, and Amanda Randles. 2019. Evaluating the Influence of Hemorheological Parameters on Circulating Tumor Cell Trajectory and Simulation Time. In *Proceedings of ACM Conference (Conference'17).* ACM, New York, NY, USA, 10 pages. https://doi.org/10.1145/nnnnnnn.nnnnnnn

Permission to make digital or hard copies of part or all of this work for personal or classroom use is granted without fee provided that copies are not made or distributed for profit or commercial advantage and that copies bear this notice and the full citation on the first page. Copyrights for third-party components of this work must be honored. For all other uses, contact the owner/author(s).
Conference'17, July 2017, Washington, DC, USA
© 2019 Copyright held by the owner/author(s).
ACM ISBN 978-x-xxxx-xxxx-x/YY/MM.
https://doi.org/10.1145/nnnnnnn.nnnnnnn

1 INTRODUCTION

Metastatic cancer is the primary cause of cancer mortality, which is the second-leading cause of death globally [1]. Metastasis is driven by the escape and transport of circulating tumor cells (CTCs) through the bloodstream to form secondary tumors in distant parts of the body. CTCs have been shown to be useful for many applications, such as the detection of non-hematological cancers [2], the ability to provide a biological understanding of malignant cells, and potentially guide towards targeted therapies [3]. Studies have shown that the knowledge of local hemodynamics can explain many metastatic sites [4] and that CTCs tend to arrest in the microvasculature [5], where likelihood of adhesion to the vessel wall and subsequent escape is heavily affected by CTC margination. Because more time near a vessel wall increases the probability of CTC extravasation, it is important to understand how certain hemorheological parameters can affect CTC movement. Simulations provide the unique opportunity to track a CTC's trajectory through the vascular system, which is not possible today *in vivo*, but to also tune one parameter at a time to determine its effect on the process.

At the micro-scale, studies have shown that the non-Newtonian behavior of blood plays an important role on its viscosity and movement of red blood cells (RBCs) [6]. Thus, in order to capture the full dynamics of CTC trajectory in the microvasculature, we expect that explicitly modeling the CTC and neighboring RBC interactions is important to capture the full dynamics of CTC movement, whereas using bulk flow parameters would not effectively reproduce micron-scale interactions. However, including cells increases simulation time by introducing both fluid-cell and cell-cell interactions, and this computational burden grows geometrically as the vessel size and number of cells increase. Additionally, accounting for the randomness of CTC and RBC distributions and the potential variance in CTC trajectory requires many simulations with the same set of parameters.

One of the cell-cell interactions that must be included when simulating cellular flow in microvessels is aggregation, which has been found to influence the distribution of RBCs [7]. In blood flow, RBCs can reversibly attach to other RBCs at low shear rates or static flow. As the shear rate is increased, stacks of RBCs break apart, demonstrating that the aggregation forces are relatively weak compared to the fluid forces. At the microvessel scale, it has been shown that aggregation tends to blunt velocity profiles and increase apparent viscosity [8].

Many previous studies have included aggregation for microvessel-scale simulations. Differences in blood viscosity in microvessels has been predicted at varying shear rates and hematocrit due to the presence of aggregation [9, 10]. Numerical studies of the motion and deformation of RBCs conducted in stenoses [11, 12] show

significant differences in downstream RBC motion at increasing aggregation strength. The effects of varying levels of RBC aggregation on viscosity and size of the cell-free layer were also explored in 2D [13–15]. These works show that RBC aggregation has a significant effect on the bulk flow at low shear rates in the microvasculature and therefore these interactions must be considered when simulating CTC motion in this regime.

Recently, computational studies tracking tumor cell margination in microvessels have been performed based on varying cell and vessel parameters [16, 17]. Additionally, the impact of varying hematocrit and microvessel size on likelihood of CTC bonding to the wall has been simulated in [18]; however, in this work, aggregation is only considered at a single vessel size and hematocrit level.

Similarly, margination of other microparticles, such as leukocytes, has been studied computationally. Leukocyte margination was shown to be negligible at high arteriole shear rates [19], but increased at low shear rates [20] and at raised hematocrit [21, 22]. Elevating the presence of RBC aggregates by raising interaction strength has also been shown to increase the likelihood of leukocyte margination [23]. We are interested in seeing if similar behavior upholds with respect to CTCs.

These microparticle movement studies provide the set of hemorheological parameters that we wish to explore: RBC aggregation, hematocrit, microvessel size, and shear rate. However, only a handful of the aforementioned works discuss the computational cost of such simulations. Code efficiency and parallelization are mentioned, but are not the main focus of these studies.

In addition to computational cost, we want to account for potential stochasticity in cell movement. Although hemodynamic variables are used to describe the bulk flow, a single discrete initialization of cells is unable to capture the wide variance in cell motion at a specific set of parameters. It is important to run many simulations with varied cell positions in order to confirm a statistical average rather than report a potential outlier. In this work, we look to replicate the randomness in cell positions by holding the initial CTC radial distance from vessel center to wall constant and varying the initial angle for a single parameter set. This exposes the CTC to different sets of neighboring RBCs, which could play a role in its margination. When scaling the number of simulations up for applications such as these stochastic tests, minimizing time-to-solution is critical in order to retrieve and analyze results in a relevant timeframe.

For high-resolution CTC tracking simulations, one way to reduce computational time is to identify potential shortcuts, such as: including fewer cells, extrapolating CTC movement from smaller vessels or different flow velocities, and identifying whether the inclusion of certain interactions result in the same CTC trajectory. Adding more cells, increasing the computational domain, and considering aggregation each adds a new layer of computational cost and complexity. Thus, it is important to identify scenarios which can be simulated more efficiently by determining the critical components of the model and only including those that influence CTC trajectory while achieving the same result. For example, if the CTC motion remains the same at 10% and 30% hematocrit, this result would indicate that fewer RBCs are required to model the same outcome, thus saving computational expense. Similarly, if aggregation interactions do not play a major role in CTC movement at a certain hematocrit or microvessel size, the aggregation computations can be ignored, further decreasing simulation time.

To our knowledge, no study has quantitatively explored combinations of varying hematocrit, vessel size, and shear rate with and without RBC aggregation on CTC trajectory, along with multiple instantiations of the same conditions to produce a statistical analysis. In this work, we study idealized microvessels and quantify the effects of RBC aggregation in the context of varying hematocrit, microvessel sizes, and shear rates on CTC movement. Each set of parameters is run multiple times with varied initial cell positions to capture heterogeneity in movement. These simulations are used to identify scenarios where certain parameters can be chosen to reduce computational cost yet keep similar CTC trajectory results.

2 MODEL AND METHODS

All simulations are performed using HARVEY, a massively parallel computational fluid dynamics solver [24, 25]. Blood is modeled as a suspension of RBCs in plasma, which is treated as a Newtonian fluid. The lattice Boltzmann method (LBM) is used as the fluid dynamics solver while a finite element model (FEM) is used for the cells. These are coupled via the immersed boundary method (IBM). Finally, a Morse potential is considered for red blood cell aggregation.

2.1 Lattice Boltzmann Method

The lattice Boltzmann method is a mesoscopic approach for numerically solving the Navier-Stokes equations [26]; the fluid is represented as set of particles that move between lattice nodes in discrete timesteps. The particle distribution function $f_i(\mathbf{x}, t)$ indicates the probability of particles residing at lattice point $\mathbf{x}$ and time t with a discrete velocity $\mathbf{c}_i$. The lattice Boltzmann equation which governs the evolution of these particles for a fluid with an external force field is

$$f_i(\mathbf{x} + \mathbf{c}_i, t + 1) = (1 - \frac{1}{\tau})f_i(\mathbf{x}, t) + \frac{1}{\tau}f_i^{eq}(\mathbf{x}, t) + F_i(\mathbf{x}, t) \quad (1)$$

for an external force distribution F_i, equilibrium distribution f_i^{eq}, and relaxation time τ, assuming the LBM spatial and temporal steps to be unity. In HARVEY, the the D3Q19 velocity discretization model is implemented, while the BGK collision operator $\Omega = \frac{1}{\tau}$ is considered, resulting in a lattice speed of sound $c_s = \frac{1}{\sqrt{3}}$. Guo's forcing scheme [27] is employed for the discretization of the external field into a distribution. No-slip conditions are enforced using the halfway bounce-back boundary conditions at the vessel walls. The 0^{th} and 1^{st} moments of the distribution function, the density ρ and momentum $\rho\mathbf{v}$, are computed as

$$\rho = \sum_{i=1}^{19} f_i \quad (2)$$

and

$$\rho\mathbf{v} = \sum_{i=1}^{19} \mathbf{c}_i f_i + \frac{1}{2}\mathbf{g} \quad (3)$$

The density ρ and velocity $\mathbf{v}$ are used to calculate the equilibrium Maxwell-Boltzmann distribution. The fluid and cell dynamics are

coupled through the external force $\mathbf{g}$, which is is converted into the force distribution F_i by

$$F_i = \left(1 - \frac{1}{2\tau}\right) \omega_i \left[\frac{\mathbf{c}_i - \mathbf{v}}{c_s^2} + \frac{\mathbf{c}_i \cdot \mathbf{v}}{c_s^4}\mathbf{c}_i\right] \cdot \mathbf{g} \tag{4}$$

where ω_i are the standard D3Q19 lattice weights.

2.2 Cell Finite Element Model

Cells are represented as fluid-filled capsules with zero-thickness triangulated membranes, derived from successive subdivisions of an icosahedron [28]. The RBC and CTC meshes are shown in Figure 1. The membrane model includes elasticity and bending stiffness [29]. The shear and dilational elastic responses of the membrane are governed by the Skalak constitutive law, where the elastic energy W is computed by

$$W = \frac{G}{4}\left(I_1^2 + 2I_1 - 2I_2 + CI_2^2\right) \tag{5}$$

for strain invariants I_1, I_2, shear elastic modulus G, and the ratio of dilational to shear modulus C [30]. A C^0 finite element model is used to compute the membrane forces from the strain energy function [31] while the Helfrich formulation is used to model membrane's bending resistance [32].

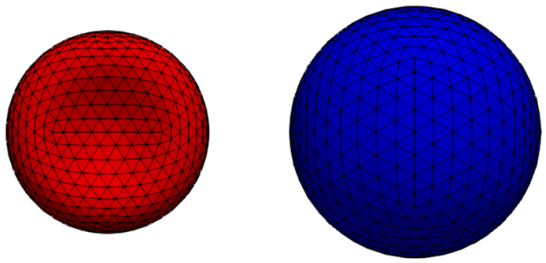

Figure 1: Triangulated RBC and CTC meshes. The RBC is generated as an 8 μm diameter biconcave disk, while the CTC is modeled as a 10 μm diameter spherical capsule. Both contain 642 vertices and 1280 triangular elements.

2.3 Immersed Boundary Method

The immersed boundary method is used to couple the Langrangian cell response with the Eulerian fluid flow by using spreading and interpolation operations to transfer data between the two systems.

First, the velocity of a cell vertex $\mathbf{V}$ is interpolated from the velocities $\mathbf{v}$ of surrounding fluid points $\mathbf{x}$ using

$$\mathbf{V}(\mathbf{X}, t) = \sum_{\mathbf{x}} \mathbf{v}(\mathbf{x}, t)\delta(\mathbf{x} - \mathbf{X}(t)) \tag{6}$$

Next, the position of the cell vertex is updated using the no-slip condition,

$$\mathbf{X}(t+1) = \mathbf{X}(t) + \mathbf{V}(t) \tag{7}$$

once again assuming unity timestep. Finally, the force $\mathbf{G}$ on a cell vertex $\mathbf{X}$ is spread onto the surrounding fluid points $\mathbf{x}$ using

$$\mathbf{g}(\mathbf{x}, t) = \sum_{\mathbf{X}} \mathbf{G}(\mathbf{X}, t)\delta(\mathbf{x} - \mathbf{X}(t)) \tag{8}$$

to define the external force $\mathbf{g}(\mathbf{x}, t)$ [33]. A four point delta support is used in this work as described in [34].

2.4 RBC Aggregation Model

In order to capture the intercellular interactions between RBCs, the Morse potential and resulting force proposed in [35] is used:

$$\phi(r) = D_e[e^{2\beta(r_0 - r)} - 2e^{\beta(r_0 - r)}] \tag{9}$$

$$f(r) = -\frac{\partial\phi(r)}{\partial r} = 2D_e\beta[e^{2\beta(r_0 - r)} - e^{\beta(r_0 - r)}] \tag{10}$$

where $\phi(r)$ and $f(r)$ are the energy and force densities per unit area respectively. Here, r represents the distance between two triangular elements on two different cells, r_0 is the zero force distance, D_e is the interaction strength, and β is a scaling factor controlling the decay of the interaction.

The aggregation force is initially calculated on an element-to-element basis, and subsequently spread onto the vertices. The total force on a single triangular element a located on cell 1 due to another cell 2 is

$$\mathbf{F}_a^{agg} = \sum_{b=1}^{N_t} f(r_{ab})(\mathbf{n}_a \cdot \mathbf{k}_1)(\mathbf{n}_b \cdot \mathbf{k}_2)A_b \tag{11}$$

where b is an element residing on cell 2, N_t is the number of triangular elements on cell 26, and r_{ab} is the distance between two elements. $\mathbf{n}_a$ and $\mathbf{n}_b$ are the outward normal unit vectors for elements a and b respectively, and $\mathbf{k}_1$ and $\mathbf{k}_2$ are the vectors connecting the center of the two cells. The dot product terms are based on Derjaguin's approximation to express the force between two curved surfaces [36, 37]. Finally, A_b is the area of triangle b, such that the total force on the cell is resolution-invariant. The force acting on a single vertex is calculated by the sum of the forces exerted on the elements that the vertex connects.

2.5 Parallelization Scheme

In HARVEY, the LBM solver is parallelized with MPI, where the simulation is decomposed into subdomains distributed to each task. Since the update step for a fluid lattice point only requires the information from adjacent points, global communication is not necessary. Neighboring tasks communicate overlapping halo regions of fluid data, transferred using non-blocking MPI calls. The cell model computations are performed in two ways: 1) the task in which the cell center resides performs the finite element model computations, and 2) the task containing a particular vertex handles the IBM interpolation step for that vertex. MPI calls are used to communicate velocities from tasks containing a cell vertex to the cell owner, and to send the vertex force calculated from the finite element model back to each task owning the vertex. A further discussion of the LBM and cell parallelizations in HARVEY can be found in previous works [25, 34].

3 RESULTS AND DISCUSSION

First, a set of experiments in shear flow is considered to capture RBC aggregation mechanics and test the interaction parameters. Then, the effects of changing hematocrit, vessel size, and shear rate on the trajectory of a CTC, in conjunction with RBC aggregation, are explored. We present results showing the average CTC radial displacement as it moves through the cylinder, as well as timing breakdowns with and without the cellular aggregation model.

3.1 Simulation Parameters and Initialization

3.1.1 Fluid Setup. The containing fluid is treated as plasma with a density of 1025 kg/m^3 and viscosity 1.2 mPa·s. Lattice grid spacing is held at a constant 0.5 µm throughout these simulations since convergence testing in [38] shows that results of RBC movement in shear flow remain similar at a grid sizing $\frac{1}{8}$ of the diameter of an RBC or smaller. Fluid boundary conditions are set using a constant inlet fluid velocity, calculated using $\dot{\gamma} = \frac{\bar{v}}{D}$ where $\dot{\gamma}$ is the shear rate, $\bar{v}$ is the average velocity of the plasma, and D is the diameter of the vessel.

3.1.2 RBC and aggregation parameters. RBC shapes are generated as stress-free biconcave disks [39] with an 8 µm diameter, consisting of 3 icosahedron refinements, leading to 642 vertices and 1280 triangular elements. This number of refinements has been shown to sufficiently capture RBC movement [38]. For the physical RBC parameters, a membrane shear elastic modulus E_s of 6×10^{-6} N/m and elastic bending modulus of 2×10^{-19} N·m is considered. For aggregation interactions, the zero force distance r_0 is chosen to be 0.49 µm along with a corresponding scaling factor β of 3.84 µm, as used by [13]. Since only nearby RBCs interact with one another, these values restrict the attractive force to only be relevant within a distance of 3.5 µm. Aggregation interactions are only applied between RBCs. Plasma, RBC, and aggregation parameters are summarized in Table 1.

Instead of searching through all of the RBCs to find those within a 3.5 µm distance at each time step, a list of neighboring cells is generated every t time steps. Due to the time step size being intrinsically tied to the lattice spacing, and a small grid size being necessary to properly apply the immersed boundary method, a cell's neighbors do not change very frequently, especially in the low shear rate regime where aggregation forces are apparent. Test runs at $\dot{\gamma} = 20$ s^{-1} conducted to determine frequency of neighbor list updates found that the minimum time between updates was above 100 timesteps, and thus $t = 100$ was chosen as a conservative value for these simulations.

3.1.3 Microvessel simulations. Microvessels are modeled as 100 µm length cylinders with varying hematocrit and diameter. The combinations of biophysical parameters tested are outlined in Figure 2. It should be noted in the smallest vessel, a maximum hematocrit of only 24% is achieved when including the CTC, and therefore the combination of 20-micron and 30% hematocrit simulations are not conducted. The first half (50 µm) is filled with RBCs based on initial hematocrit and the CTC, and the cells are allowed to flow to the end of the channel. To avoid startup costs of packing many RBCs, an arrangement of RBC 'tiles' generated by an external library [43] is used to achieve a dense packing and 'random' RBC placement.

Table 1: Plasma and RBC Parameters

Parameter	Symbol	Value
plasma density	ρ	1025 kg/m^3 [40]
plasma viscosity	μ_p	1.2 mPa·s [41]
RBC membrane shear modulus	E_s	6×10^{-6} N/m [42]
RBC bending resistance	E_b	2×10^{-19} N·m [42]
intercellular energy density	D_e	0.2 µJ/m^2 [14]
scaling factor	β	3.84 µm^{-1} [14]
zero force distance	r_0	0.49 µm [14]

The CTC is represented as a 10 micron-diameter spherical capsule surrounded by a zero-thickness shell, regulated by the Skalak constitutive law; this principle has been shown shown to sufficiently capture deformation of a spherical capsule [44]. The CTC is placed radially halfway between the center and the vessel wall. To account for variance in CTC movement due to initial cell positions, θ is varied in cylindrical coordinates for a total of 8 different CTC initial positions to provide a stochastic analysis, as shown in Figure 3a while an example initial case of the CTC at 30% hematocrit in a 30 micron diameter vessel in shown in Figure 3b.

The CTC center is tracked and presented as radial displacement (radial movement divided by vessel diameter) vs lateral movement in a variety of conditions, while the runtime is broken into time spent running LBM, IBM-FEM, and aggregation calculations. This entire workflow is summarized in Figure 4.

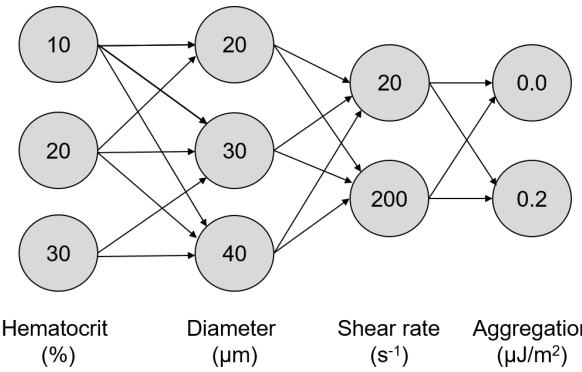

Figure 2: Biophysical parameter space explored: a combination of 3 hematocrits, 3 vessel diameters, 2 shear rates, and 2 aggregation strengths. Due to cell packing issues in the smallest vessel, we discard the 30% hematocrit in the 20 µm diameter vessel combinations, leading to a total of 32 parameter arrangements.

We expect to see approximately the same amount of time spent in the LBM calculations at constant vessel size, with some variance due to cluster performance. Also, it is important to note that increasing vessel diameter and/or hematocrit allows more RBCs to be placed. The amount of time spent in the IBM-FEM calculations is expected to scale linearly with number of RBCs. Since aggregation performs cell-to-cell calculations, the increase in aggregation runtime is expected to scale on the order of $O(n^2)$ with the number of

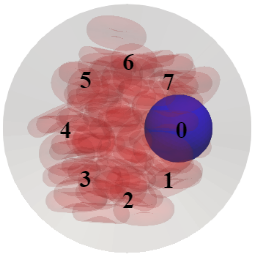

(a) Initial positions of the CTC, holding r constant and varying θ. The CTC is placed in 8 different equally-spaced angular positions to capture stochasticity.

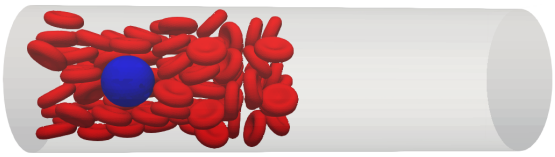

(b) Example 30 micron diameter vessel at 30% hematocrit with CTC positioned at x=25 μm.

Figure 3: Initial setup for microvessel simulations.

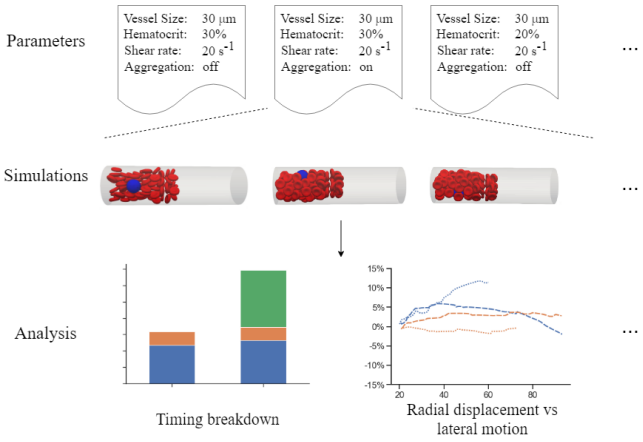

Figure 4: Visualization of the workflow: parameter assignment, parallel distribution of stochastic simulations, and CTC motion and timing analysis.

RBCs. However, both a cutoff distance and neighbor list are applied such that this is bounded by $O(n \log n)$; however, the latter heavily depends on initial placement and distance between cells.

3.1.4 Compute Architectures. The full set of simulations were performed on an Intel-based cluster, with dual-socket compute nodes connected with 56Gb/s Infiniband interconnect. Each node has two Intel Xeon E5-2695V4 Broadwell processors with 40 CPU cores. Each simulation was conducted using a distributed memory scheme on a single node across 40 tasks. Our application is compiled with the 2018 versions of the Intel C++ compiler and MPI library.

3.2 Testing Aggregation in Shear Flow

To verify the aggregation model in the presence of flow, we run a set of tests with cells placed in infinite shear flow. Previous works have tested a wide span of D_e ranging from 0.052 (very weak) to 10.0 (extremely strong) μJ/m^2 [11, 12, 14, 45]. We proceed with the shear flow experiments applying a moderate aggregation strength of $D_e = 0.2$ μJ/m^2.

Four cells are placed in a domain with dimensions 50 μm by 20 μm by 10 μm where different shear rates and aggregation strengths are considered. Shear flow boundary conditions are implemented at the top (x=25 μm) and bottom (x=−25 μm) of the simulation domain by choosing equal but opposite velocities. Previous works have shown that at shear rates under approximately 50 s^{-1}, aggregation forces become relevant and cause an increase in blood viscosity [22]; thus, shear rates of 20 s^{-1} and 100 s^{-1} were chosen for shear flow tests.

Figures 5a and 5b show the movement of the cells in 20 s^{-1} when zero and moderate aggregation is considered, respectively. In the case of zero aggregation, the cells separate easily. When aggregation is activated, the cells initially come closer to each other until they break into two sets of aggregates, qualitatively agreeing with the results of [13].

At 100 s^{-1} with no aggregation, the movement of the cells follows the same pattern as that at 20 s^{-1}, shown in Figure 5c. Figure 5d shows the movement of the four cells with moderate aggregation at 100 s^{-1}. At the high shear rate, fluid forces dominate the intercellular forces and pull the cells apart before they can move closer. The cells disperse in a similar manner to the zero aggregation case.

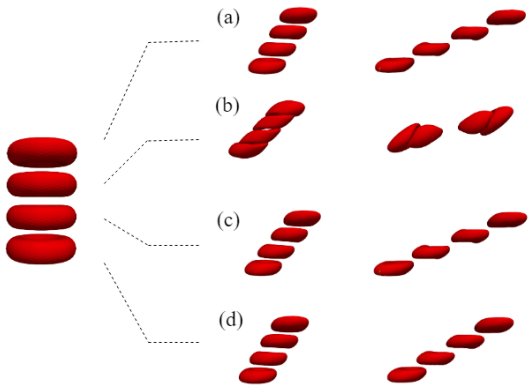

Figure 5: Aggregation testing at shear rates 20 s^{-1} and 100 s^{-1}. Cases of (a) zero aggregation at 20 s^{-1} (b) moderate aggregation at 20 s^{-1} (c) zero aggregation at 100 s^{-1} (d) moderate aggregation at 100 s^{-1}

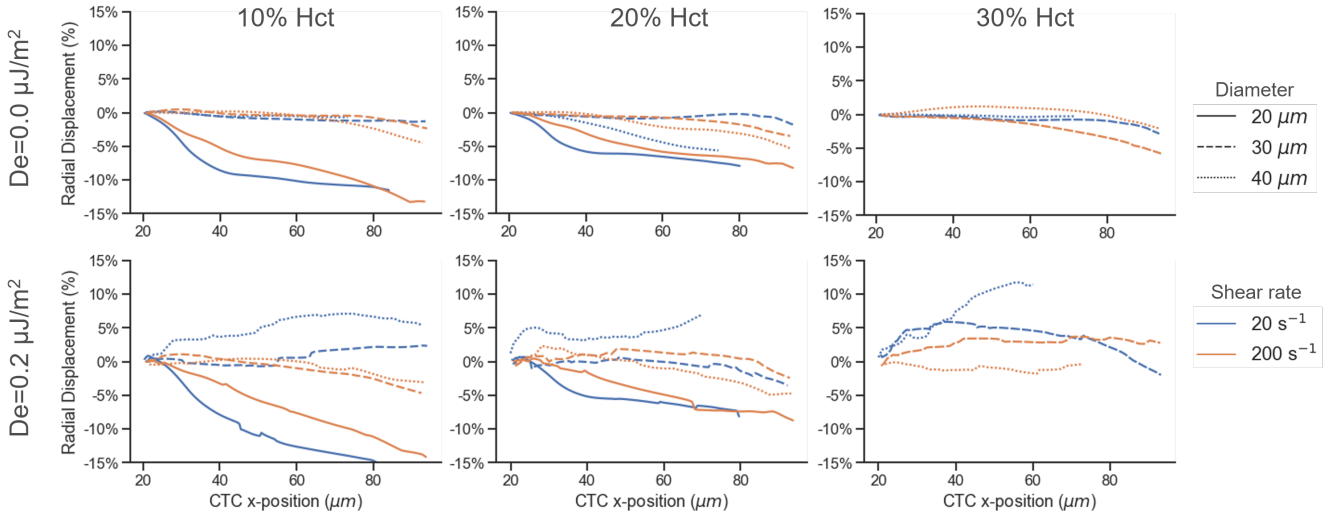

Figure 6: Breakdown of radial CTC displacement vs lateral movement at 10%, 20%, and 30% hematocrit with and without RBC aggregation

3.3 Effect of hematocrit and aggregation on CTC trajectory

Due to the Fahreus effect, hematocrit in the microvasculature tends to drop below systemic levels. Using Pries equation [46], a systemic hematocrit of 40-45% corresponds to a tube hematocrit of approximately 30% for a 20 to 40 μm diameter microvessel. As previously mentioned, an increased number of RBCs introduces a higher computational burden, leading to longer runtimes. If the trajectory of a CTC remains statistically the same at varying hematocrits, modeling fewer RBCs is needed to capture the same motion and would be computationally more efficient. Thus, simulations up to a hematocrit of 30% are conducted.

First, CTC trajectory at 10%, 20%, and 30% hematocrit (Hct) without aggregation is considered, pictured in the top row of Figure 6. Specifically in the 20 μm diameter vessel, there is significant movement towards the center of the vessel, but less pronounced in the 20% compared to the 10% case. In the other cases, at all 3 hematocrits, the CTC remains within 5% radial displacement. Therefore with no aggregation, as hematocrit is increased, there is a decrease in inward CTC radial motion.

When aggregation is introduced, CTC movement is heavily affected, as shown in the bottom row of Figure 6. At 10% Hct, the CTC acts similarly to its no-aggregation case, except at the low shear 30 and 40 micron diameter cases, where there is an increase in outward radial movement. As the hematocrit is increased to 20% and 30%, margination occurs faster in the aforementioned cases. This phenomenon can be explained by the RBC aggregates converging towards the center of the vessel and pushing the CTC outwards, which is consistent with previous simulation work [18]. We speculate that the CTC in the 10% Hct case tends not to marginate because the RBCs are too spaced out to form multiple aggregates and force the CTC radially outward. Thus, when including aggregation in the simulations, we find that CTC trajectory increases in the radial outward direction.

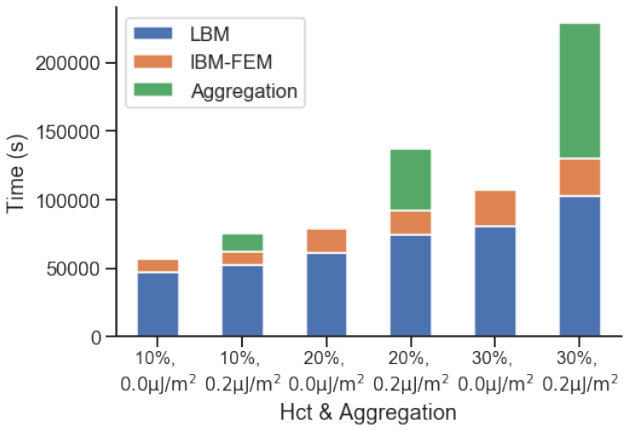

Figure 7: Breakdown of time spent performing LBM, IBM-FEM, and aggregation calculations at 10%, 20%, and 30% hematocrit with and without aggregation considered. Both hematocrit and aggregation strength have an effect on CTC trajectory.

The runtime breakdowns both with and without aggregation are presented in Figure 7. The time spent running the LBM computations is approximately the same throughout, while IBM-FEM computation time scaled linearly with cells added. At each hematocrit, including aggregation did not change the LBM and IBM-FEM times since the initial number of fluid points and cells remains the same. For the simulations with aggregation considered, the aggregation runtime increased from under 20% of total runtime at 10% Hct to about half of the total runtime at 30% Hct. The aggregation function begins to dominate simulation time very quickly. Although its current implementation is not fully optimized, the inclusion of aggregation still adds a nonzero overhead to the simulations.

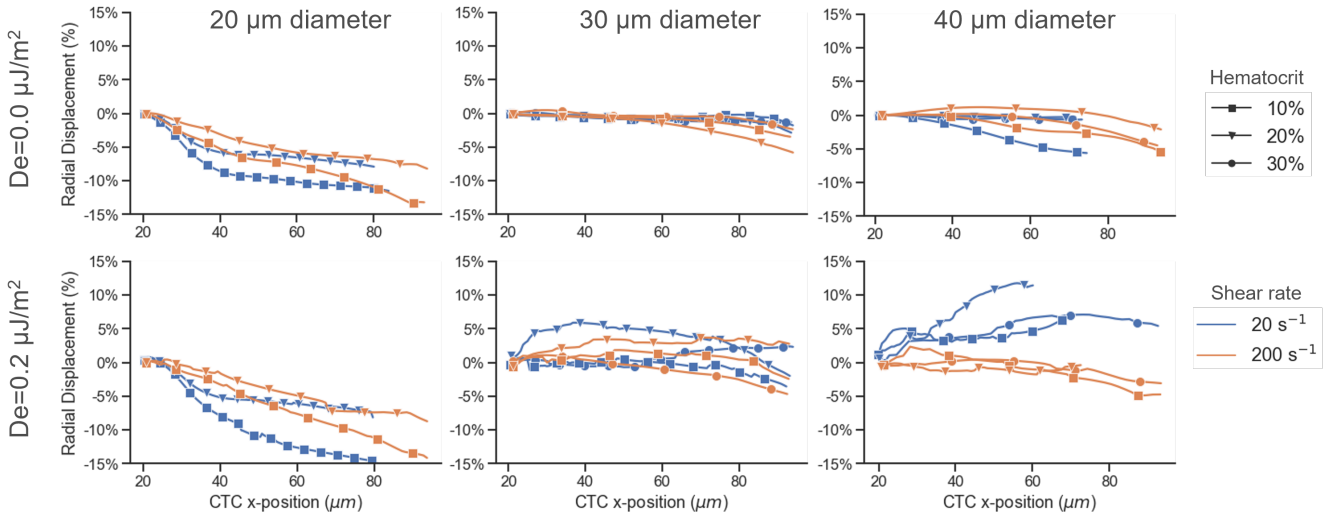

Figure 8: Breakdown of radial CTC displacement vs lateral movement in 20 μm, 30 μm, and 40 μm diameter microvessels with and without RBC aggregation. Both diameter and aggregation strength have an effect on CTC trajectory.

These results show that varying hematocrit and including aggregation significantly affect CTC trajectory such that lowering the RBC count or disregarding aggregation will not produce the same set of CTC trajectories when running these simulations. Therefore taking both hematocrit in combination with aggregation into account is critical to determine accurate CTC paths.

3.4 Effect of microvessel diameter and aggregation on CTC trajectory

As noted in [13], blood should be treated as a non-Newtonian fluid in vessels with diameters under 200 μm. At this scale, the non-Newtonian effects play a significant role in the rheology. In simulations, including both the cell and aggregation models introduces another level of computational expense. If CTC movement in larger vessels can be estimated from its path in smaller vessels, one method of potentially minimizing this time would be to simulate very small vessels and extrapolate CTC trajectory in larger vessels based on the results.

Increasing the diameter of the cylindrical vessel by a factor of n results in an increase in volume, and number of lattice points, by a factor of n^2 if the length of the vessel is held constant. Additionally, an increase in volume requires more cells to maintain the same level of hematocrit, leading to more IBM-FEM and aggregation calculations. Therefore in this set of simulations, we test CTC trajectory in a set of microvessel sizes ranging from 2.5 to 5 times the diameter of an RBC. We expect that in vessels smaller than the RBC diameter, the single file RBCs would play a different role in CTC movement and therefore diameters of 20, 30, and 40 μm.

Results for CTC trajectory without aggregation are presented in the top row of Figure 8. At a 20 μm diameter, the CTC consistently displays a radial motion towards the center of the vessel. In the 30 μm vessel, the CTC tends to stay in a radially constant position while in the 40 μm diameter vessel, the CTC shows a bit more variation in motion, but still within 5% displacement towards the center. Therefore as diameter is increased without considering aggregation, the CTC tends to stay in a radially constant position.

When aggregation is introduced, CTC trajectory is affected in the larger vessels, as shown in the bottom row of Figure 8. For the 20 μm diameter vessel, there is little change in CTC motion. However, in both of the 30 μm and 40 μm vessels, the CTC marginates towards the vessel wall, but more quickly in the 40 μm case at the low shear rates.

These results show that at varying microvessel size, the radial displacement of the CTC does not scale with the size of the vessel. Furthermore, including aggregation has a notable effect on CTC movement. Thus vessel size and aggregation must be included to determine CTC trajectory at these hematocrits and shear rates.

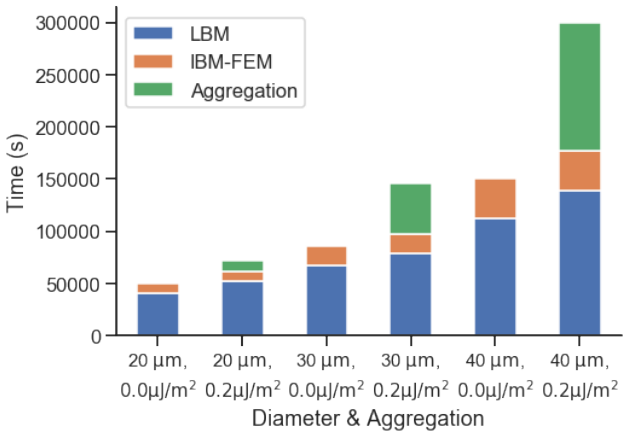

Figure 9: Breakdown of time spent performing LBM, IBM-FEM, and aggregation calculations in 20 μm, 30 μm, and 40 μm diameter microvessels.

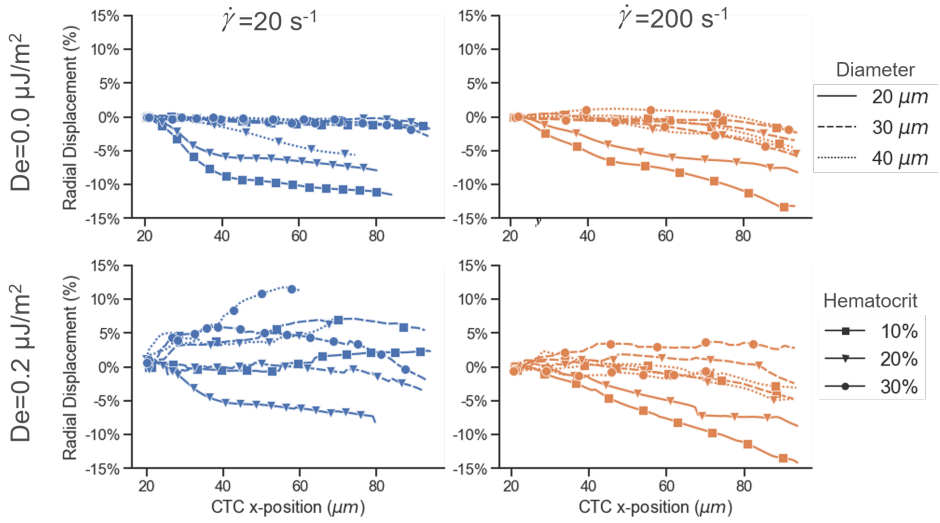

Figure 10: Breakdown of radial CTC displacement vs lateral movement at shear rates $20\,s^{-1}$ and $200\,s^{-1}$ with and without RBC aggregation. Aggregation strength only has an effect on CTC trajectory at the low shear rate.

The timing breakdowns for these simulations are displayed in Figure 9. At constant vessel size with and without aggregation, the LBM and IBM-FEM runtimes remain similar. As the vessel size increases, the LBM and IBM-FEM time increases linearly with the volume as the number of grid points and the number of RBCs increase. Aggregation calculations scale up from about 10% of total runtime in the 20 μm diameter vessel to almost 50% of the simulation time in the 40 μm case.

3.5 Effect of shear rate and aggregation on CTC trajectory

RBC aggregation only plays a major role in the viscosity at the lower end of microvascular shear rates. However, in regions of the vessel where the flow is slow, aggregates still might form, especially at higher hematocrit, which could affect the movement of a particular cell. Although aggregation might not affect bulk parameters, it could still affect CTC margination. Therefore we choose two shear rates, $20\,s^{-1}$ and $200\,s^{-1}$, to test CTC trajectory.

CTC movement at $\dot{\gamma} = 20\,s^{-1}$ and $\dot{\gamma} = 200\,s^{-1}$ is presented in Figure 10. The top row displays the CTC trajectories run at zero and moderate RBC aggregation, respectively. At the low shear rate, the inclusion of the aggregation model makes a major difference on the CTC trajectory. Without it, the CTC either remains radially constant or moves towards the center of the vessel. However, when aggregation is considered, there is an increase in outward radial displacement in almost every case. At the higher shear rate, where the aggregation forces are dominated by the fluid forces, the CTC trajectory remains approximately the same: for both the zero and moderate aggregation cases at $\dot{\gamma} = 200\,s^{-1}$, the CTC shows little change in radial displacement.

Thus, aggregation does not need to be considered at high shear rates, resulting in simulation speed up while retaining similar results. Figure 11 provides the timing breakdown for both shear rates. By dismissing the aggregation interactions for the high shear rate

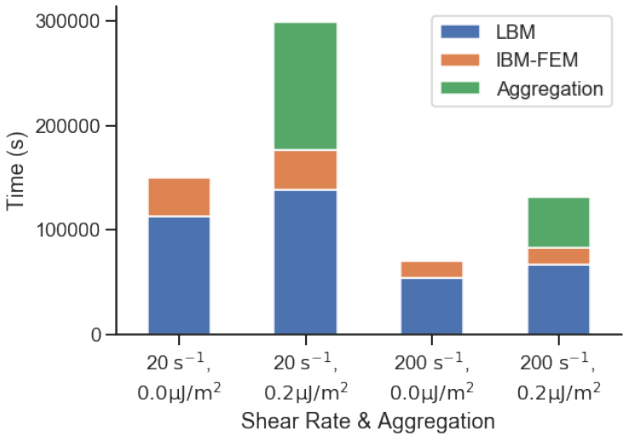

Figure 11: Breakdown of time spent performing LBM, IBM-FEM, and aggregation calculations at shear rates $20\,s^{-1}$ and $200\,s^{-1}$ with and without aggregation considered.

simulations, the runtime of these 3 parts of the model drops from approximately 131,000 seconds to 83,000 seconds - a 37% time savings on average - visualized on the right two bars. Note that the real time simulation bars for the $\dot{\gamma} = 200\,s^{-1}$ case are smaller because the cell traveled the lateral distance faster.

4 CONCLUSIONS

CTCs are derived from the escape of a tumor cell into the blood stream from the original tumor. These CTCS flow through the blood and are transported to distant organs via the vascular or lymphatic system to form secondary tumors. During circulation, a CTC endures hydrodynamic and interaction forces, and its path heavily depends on the stresses caused by the fluid and its interactions with

neighboring cells, especially within the microvasculature. Therefore simulations of CTC movement in microvessels require explicit modeling of the CTC, surrounding RBCs, and their interactions.

In microvessel simulations, including cells raises simulation time due to the introduction of both fluid-cell and cell-cell interactions. Adding the calculation of red blood cell aggregation further increases the total runtime of the simulation, which scales geometrically as more cells are introduced. This study looks for methods to reduce computational cost by testing the effects of aggregation, hematocrit, vessel size, and shear rate on the movement of a CTC in microvessels. To capture the diversity in initial cell positions and provide stochastic testing, a framework to run and analyze many simulations with altered CTC positions is developed.

The results from this work show that at 10-30% hematocrit, CTC movement is significantly altered in the presence of more RBCs and with aggregation. Similarly, at varying microvessel sizes, CTC motion cannot be extrapolated from its movement in a smaller vessel. Although these simulations require extra computational cost, hematocrit, vessel size, and aggregation must be accounted to produce accurate CTC trajectories. At low shear rates, aggregation plays a considerable role in determining the CTC path, but at high shear rates, aggregation only has a minor effect. Therefore at high shear rates, aggregation calculations can be disregarded, saving about 40% runtime on average in this set of simulations.

In future work, we plan to further optimize the aggregation function and explore the effect of the number of processors on the LBM, IBM-FEM, and aggregation runtimes. This work identifies some of the hemorheological parameters required to properly capture CTC motion and sets up the stochastic testing framework for future CTC tracking simulations in various flow regimes in microvessels.

REFERENCES

[1] WHO. Cancer 12. *Cancer*, (September 2018):2018, 2018.

[2] Matthew G Krebs, Robert L Metcalf, Louise Carter, Ged Brady, Fiona H Blackhall, and Caroline Dive. Molecular analysis of circulating tumour cellsâĂŤbiology and biomarkers. *Nature Reviews Clinical Oncology*, 11(3):129–144, 2014.

[3] Pravin D Potdar and Navjeet Kaur Lotey. Role of circulating tumor cells in future diagnosis and therapy of cancer. 1(2), 2015.

[4] Leonard Weiss. Comments on hematogenous metastatic patterns in humans as revealed by autopsy. *Clinical & Experimental Metastasis*, 10(3):191–199, may 1992.

[5] Gautier Follain, Naël Osmani, Ana Sofia Azevedo, Guillaume Allio, Luc Mercier, Matthia A. Karreman, Gergely Solecki, Maria Jesùs Garcia Leòn, Olivier Lefebvre, Nina Fekonja, Claudia Hille, Vincent Chabannes, Guillaume Dollé, Thibaut Metivet, François Der Hovsepian, Christophe Prudhomme, Angélique Pichot, Nicodème Paul, Raphaël Carapito, Siamak Bahram, Bernhard Ruthensteiner, André Kemmling, Susanne Siemonsen, Tanja Schneider, Jens Fiehler, Markus Glatzel, Frank Winkler, Yannick Schwab, Klaus Pantel, Sébastien Harlepp, and Jacky G. Goetz. Hemodynamic Forces Tune the Arrest, Adhesion, and Extravasation of Circulating Tumor Cells. *Developmental Cell*, 45(1):33–52.e12, apr 2018.

[6] Aleksander S Popel and Paul C Johnson. Microcirculation and Hemorheology. *Annual review of fluid mechanics*, 37:43–69, jan 2005.

[7] S Chien, S Usami, R J Dellenback, and M I Gregersen. Shear-dependent interaction of plasma proteins with erythrocytes in blood rheology. *American Journal of Physiology-Legacy Content*, 219(1):143–153, 1970.

[8] Oguz K Baskurt and Herbert J Meiselman. Erythrocyte aggregation: Basic aspects and clinical importance. *Clinical Hemorheology and Microcirculation*, 53(1-2):23–37, 2013.

[9] Dmitry A Fedosov. Simulations of Blood Flow on the Cell Scale. pages 1–22.

[10] Dmitry A Fedosov, Wenxiao Pan, Bruce Caswell, Gerhard Gompper, and George E Karniadakis. Predicting human blood viscosity in silico. *Proceedings of the National Academy of Sciences*, 108(29):11772 LP – 11777, jul 2011.

[11] Koohyar Vahidkhah, Peter Balogh, and Prosenjit Bagchi. Flow of Red Blood Cells in Stenosed Microvessels. *Scientific reports*, 6:28194, jun 2016.

[12] L L Xiao, C S Lin, S Chen, Y Liu, B M Fu, and W W Yan. Effects of red blood cell aggregation on the blood flow in a symmetrical stenosed microvessel. *Biomechanics and Modeling in Mechanobiology*, 2019.

[13] Junfeng Zhang, Paul C. Johnson, and Aleksander S. Popel. Red blood cell aggregation and dissociation in shear flows simulated by lattice Boltzmann method. *Journal of Biomechanics*, 41(1):47–55, 2008.

[14] Junfeng Zhang, Paul C Johnson, and Aleksander S Popel. Effects of erythrocyte deformability and aggregation on the cell free layer and apparent viscosity of microscopic blood fl ows. 77:265–272, 2009.

[15] Junfeng Zhang. Effect of Suspending Viscosity on Red Blood Cell Dynamics and Blood Flows in Microvessels. *Microcirculation*, 18(7):562–573, oct 2011.

[16] Naoki Takeishi, Yohsuke Imai, Takami Yamaguchi, and Takuji Ishikawa. Flow of a circulating tumor cell and red blood cells in microvessels. *Physical Review E*, 92(6):63011, dec 2015.

[17] Michael R King, Kevin G Phillips, Annachiara Mitrugno, Tae-Rin Lee, Adelaide M E de Guillebon, Siddarth Chandrasekaran, Matthew J McGuire, Russell T Carr, Sandra M Baker-Groberg, Rachel A Rigg, Anand Kolatkar, Madelyn Luttgen, Kelly Bethel, Peter Kuhn, Paolo Decuzzi, and Owen J T McCarty. A physical sciences network characterization of circulating tumor cell aggregate transport. *American journal of physiology. Cell physiology*, 308(10):C792–C802, may 2015.

[18] Lanlan Xiao, Yang Liu, Shuo Chen, and Bingmei Fu. Simulation of Deformation and Aggregation of Two Red Blood Cells in a Stenosed Microvessel by Dissipative Particle Dynamics. *Cell Biochemistry and Biophysics*, pages 513–525, 2016.

[19] Naoki Takeishi, Yohsuke Imai, Keita Nakaaki, Takami Yamaguchi, and Takuji Ishikawa. Leukocyte margination at arteriole shear rate. *Physiological reports*, 2(6):e12037, jun 2014.

[20] Dmitry A Fedosov, Julia Fornleitner, and Gerhard Gompper. Margination of White Blood Cells in Microcapillary Flow. *Physical Review Letters*, 108(2):28104, jan 2012.

[21] Jonathan B Freund. Leukocyte margination in a model microvessel. *Physics of Fluids*, 19(2):1–13, 2007.

[22] Katherine B Abbitt and Gerard B Nash. Rheological properties of the blood influencing selectin-mediated adhesion of flowing leukocytes. *American Journal of Physiology-Heart and Circulatory Physiology*, 285(1):H229–H240, jul 2003.

[23] Chenghai Sun and Lance L Munn Ã. Influence of erythrocyte aggregation on leukocyte margination in postcapillary expansions : A lattice Boltzmann analysis. 362:191–196, 2006.

[24] Amanda Peters Randles, Laxmikant V Kale, Jeff Hammond, William D Gropp, and Efthimios Kaxiras. Performance analysis of the lattice Boltzmann model beyond Navier-Stokes , oct 2013.

[25] Amanda Randles, Erik W. Draeger, and Peter E. Bailey. Massively Parallel Simulations of Hemodynamics in the Primary Large Arteries of the Human Vasculature. *Journal of Computational Science*, 9:70–75, 2015.

[26] Shiyi Chen and Gary D Doolen. LATTICE BOLTZMANN METHOD FOR FLUID FLOWS. *Annual Review of Fluid Mechanics*, 30(1):329–364, jan 1998.

[27] Zhaoli Guo, Chuguang Zheng, and Baochang Shi. Discrete lattice effects on the forcing term in the lattice Boltzmann method. *Physical Review E*, 65(4):46308, apr 2002.

[28] T Krüger, F Varnik, and D Raabe. Efficient and accurate simulations of deformable particles immersed in a fluid using a combined immersed boundary lattice Boltzmann finite element method. *Computers & Mathematics with Applications*, 61(12):3485–3505, 2011.

[29] John Gounley, Erik W Draeger, and Amanda Randles. Numerical simulation of a compound capsule in a constricted microchannel. *Procedia Computer Science*, 108:175–184, 2017.

[30] J Walter, A.-V. Salsac, D Barthès-Biesel, and P Le Tallec. Coupling of finite element and boundary integral methods for a capsule in a Stokes flow. *International Journal for Numerical Methods in Engineering*, 83(7):829–850, jul 2010.

[31] S Shrivastava and J Tang. Large deformation finite element analysis of non-linear viscoelastic membranes with reference to thermoforming. *The Journal of Strain Analysis for Engineering Design*, 28(1):31–51, jan 1993.

[32] W Helfrich. Elastic Properties of Lipid Bilayers: Theory and Possible Experiments. *Z. Naturforsch. C*, 28, dec 1973.

[33] Charles S. Peskin. Peskin, C.S.: The immersed boundary method. Acta Numerica 11, 479-517. *Acta Numerica*, 11:479–517, jan 2002.

[34] John Gounley, Erik Draeger, and Amanda Randles. Immersed Boundary Method Halo Exchange in a Hemodynamics Application. pages 441–455. jun 2019.

[35] Yaling Liu, Lucy Zhang, Xiaodong Wang, and Wing Kam Liu. Coupling of Navier âĂŞ Stokes equations with protein molecular dynamics and its application to hemodynamics âĂą. (October 2003):1237–1252, 2004.

[36] B Chung, P C Johnson, and A S Popel. Application of Chimera grid to modelling cell motion and aggregation in a narrow tube. (June 2006):105–128, 2007.

[37] Subir Bhattacharjee, Menachem Elimelech, and Michal Borkovec. DLVO Interaction between Colloidal Particles: Beyond Derjaguin's Approximation. *Croatica Chemica Acta*, 71(4):883–903, 1998.

[38] Huilin Ye and Zhiqiang Shen. Interplay of deformability and adhesion on localization of elastic micro-particles in blood flow. (February), 2019.

[39] C Pozrikidis. Numerical simulation of the flow-induced deformation of red blood cells. *Annals of Biomedical Engineering*, 31(10):1194–1205, 2003.

[40] Bruce C McLeod and AABB. *Apheresis : principles and practice*. AABB Press, Bethesda, Md., 2010.
[41] Richard Skalak and Shu Chien. *Handbook of bioengineering*. McGraw-Hill New York, 1987.
[42] Richard Waugh and R M Hochmuth. Chapter 60: mechanics and deformability of hematocytes. *Biomedical Engineering Fundamentals*, pages 60–63, aug 2002.
[43] E G Birgin, R D Lobato, and J M Martinez. A Nonlinear Programming Model with Implicit Variables for Packing Ellipsoids. *J. of Global Optimization*, 68(3):467–499, jul 2017.
[44] Dominique Barthès-Biesel, Anna Diaz, and Emmanuelle Dhenin. Effect of constitutive laws for two-dimensional membranes on flow-induced capsule deformation. *Journal of Fluid Mechanics*, 460:211–222, 2002.
[45] Ting Ye, Nhan Phan-thien, Boo Cheong Khoo, Chwee Teck Lim, Ting Ye, Nhan Phan-thien, Cheong Khoo, and Chwee Teck Lim. Dissipative particle dynamics simulations of deformation and aggregation of healthy and diseased red blood cells in a tube flow Dissipative particle dynamics simulations of deformation and aggregation of healthy and diseased red blood cells in a tube flow. 111902(2014), 2017.
[46] A R Pries, D Neuhaus, and P Gaehtgens. Blood viscosity in tube flow: dependence on diameter and hematocrit. *American Journal of Physiology-Heart and Circulatory Physiology*, 263(6):H1770–H1778, dec 1992.